Article | Open Access

Energy Materials

Wang *et al. Energy Mater.* **2026**, *6*, 600114 **DOI:**10.20517/energymater.2026.178

Efficient solar-driven interfacial steam-hydropower co-generation by high-quality carbon nanotube from discarded polyolefin separator

Huiyue Wang, Mengjie Xu, Xueying Wen, Guixin Hu, Qianyu Wei, Lingling Feng, Xinyao Zhang, Ran Niu, Jiang Gong*

Keywords:
Interfacial solar steam generation, freshwater-electricity co-generation, carbon nanotube, solar-to-thermal conversion, discarded polyolefin separators

Citation: Wang, H.; Xu, M.; Wen, X.; Hu, G.; Wei, Q.; Feng, L.; Zhang, X.; Niu, R.; Gong, J. Efficient solar-driven interfacial steam-hydropower co-generation by high-quality carbon nanotube from discarded polyolefin separator. *Energy Mater.* **2026**, *6*, 600114. https://dx.doi.org/10.20517/energymater.2026.178

Received: 19 Jun 2026
First Decision: 15 Jul 2026
Revised: 28 Jul 2026
Accepted: 13 Aug 2026
Published: 8 Sep 2026

Academic Editor:
Yuping Wu
Copy Editor:
Fangling Lan
Production Editor:
Fangling Lan

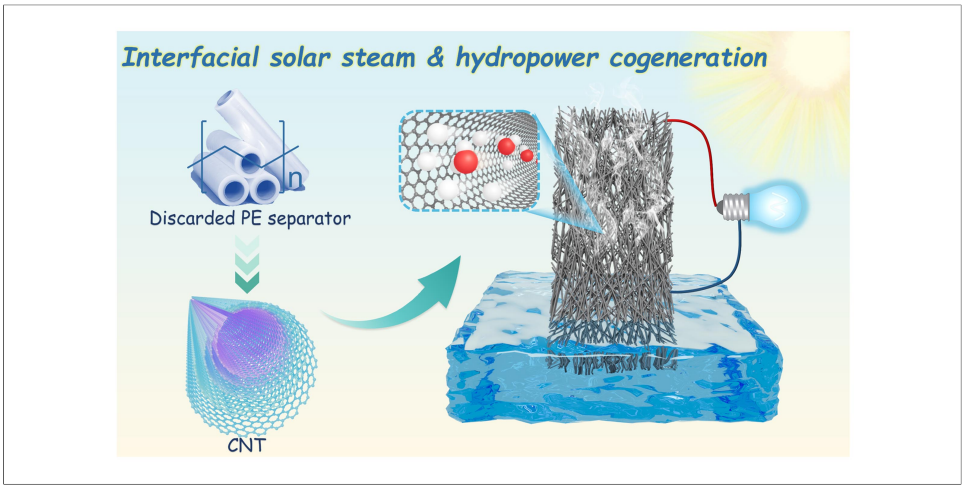

Abstract

Converting discarded polyolefin separators into valuable carbon nanotubes (CNTs) not only contributes to the high-value utilization of discarded separators, but also offers a green approach to construct advanced CNT-based generators. However, the controlled carbonization of discarded polyolefin separators into high-quality CNTs remains challenging, and the mechanism of electricity generation in CNTs remains obscure. Herein, we report the "all-in-one" catalytic strategy using multi-component Ni/Mo/Mg catalysts to realize the controllable carbonization of discarded polyolefin separators into high-quality CNTs. By adding Mo and Mg to Ni in a molar ratio of 5/0.1/0.5 (Ni/Mo/Mg), the catalyst displays high catalytic activity, dispersion, and stability, and achieves a CNT yield of 57.4 wt%. Thanks to the good photothermal conversion capability and excellent wettability, the CNT evaporator achieves an evaporation rate of 2.73 kg m^{-2} h^{-1}, a photo-to-thermal efficiency of 95.4%, and an open-circuit voltage of 0.221 V under laboratory conditions, which ranks as one of the most efficient evaporators/generators. In practical experiments, the total water production and voltage output are 2.51 kg m^{-2} over 5 h and

Key Laboratory of Material Chemistry for Energy Conversion and Storage, Ministry of Education, Hubei Key Laboratory of Material Chemistry and Service Failure, School of Chemistry and Chemical Engineering, Huazhong University of Science and Technology, Wuhan 430074, Hubei, China.

***Correspondence to:** Prof. Jiang Gong, Key Laboratory of Material Chemistry for Energy Conversion and Storage, Ministry of Education, Hubei Key Laboratory of Material Chemistry and Service Failure, School of Chemistry and Chemical Engineering, Huazhong University of Science and Technology, Wuhan 430074, Hubei, China. E-mail: gongjiang@hust.edu.cn

0.215-0.265 V, respectively. Molecular dynamics simulation results show that the surface functional groups interact more strongly with H^+ than with OH^-. With the continuous evaporation of bulk water, H^+ moves faster upward along the nanochannel than OH^-, thus forming a potential difference. This study provides an eco-friendly route for synthesizing advanced carbon nanomaterials and co-generating freshwater and electricity.

INTRODUCTION

With the rapid advancement of the global energy transformation strategy, the lithium-ion battery industry has shown explosive growth[1-3]. During the industrial production of polyolefin battery separators, discarded polyolefin separators are generated when they fail to meet the requisite quality standards[4] and are unsuitable for use as lithium-ion battery separators. Typically, these discarded polyolefin separators are produced in large volumes and possess a uniform composition with high purity. However, they are predominantly sold as raw plastic materials at a relatively low price. By contrast, converting these discarded polyolefin separators into high-value-added products has become a green and economical upcycling strategy[5-7], expected to meet the requirements of sustainable industrial development. Interestingly, these discarded polyolefin separators are considered ideal precursors for the preparation of high-value-added carbon nanotubes (CNTs)[8-10] due to their high purity, high carbon content, and low cost. However, the pyrolysis products of discarded polyolefin separators are usually complex, making it extremely difficult to precisely control the carbonization process. Additionally, during the carbonization process, carbon readily deposits on the catalyst surface, thereby deactivating the catalyst. A range of carbonization techniques have been reported to suppress carbon deposition and achieve precise tailoring of the morphology and porosity of CNTs, such as the Joule flash heating method[11], microwave-assisted carbonization[9,12,13], and combined catalyst carbonization[14]. Joule flash heating and microwave irradiation are inseparable from high-precision equipment and high energy consumption. The catalytic carbonization method can achieve the pyrolysis of polymer skeletons and the controlled growth of carbon materials by selecting appropriate catalysts[15-17]; however, additional catalysts are required to tune the morphology of the resulting carbon materials. Therefore, it is essential to rationally design a multi-in-one catalyst for converting discarded polyolefins into CNTs. Furthermore, during the upcycling process, the structure-activity relationship between the catalyst and CNT morphology remains ambiguous.

On the other hand, carbon materials are uniquely suited for solar-driven energy conversion owing to their broad-spectrum light absorption, superior thermal conductivity, and chemical stability[18-20]. By harnessing solar energy, carbon materials can enable the co-generation of multiple forms of clean energy[21,22], offering a powerful strategy to mitigate global water scarcity and the energy crisis. Specifically, interfacial solar steam generation technology achieves rapid conversion from liquid water to gaseous water by localizing photogenerated heat on the surface of photothermal materials[19,23-25]. A complex microenvironment is concomitantly formed during interfacial photothermal evaporation, thereby providing a platform for the construction of multifunctional integrated systems[26-30]. Typically, integration with hydropower technology allows for the co-generation of freshwater and electricity by harnessing environmental latent heat[31,32]. Recently, driven by the photothermal conversion and modifiable surface/interfacial chemistry of carbon materials, a variety of dual-functional evaporators have been reported to generate freshwater and power[33,34]. Wei *et al.* prepared CNT dual-functional evaporators, achieving an evaporation rate of 2.79 kg m^{-2} h^{-1} and an output voltage of 0.26 V[14]. Hu *et al.* constructed a carbon foam evaporator from waste polycarbonate, which achieved an evaporation flux of 3.03 kg m^{-2} h^{-1} and an open-circuit voltage of 0.33 V[35]. They proposed that thermal and solar energy work together to increase power output. Ding *et al.* proposed a CNT/wood generator to yield freshwater (1.19 kg m^{-2} h^{-1}) and electricity (0.35 mW m^{-2})[36]. Despite the great progress in this field[37], the synergistic mechanism for co-generating freshwater and power by dual-functional CNT-based evaporators remains underexplored.

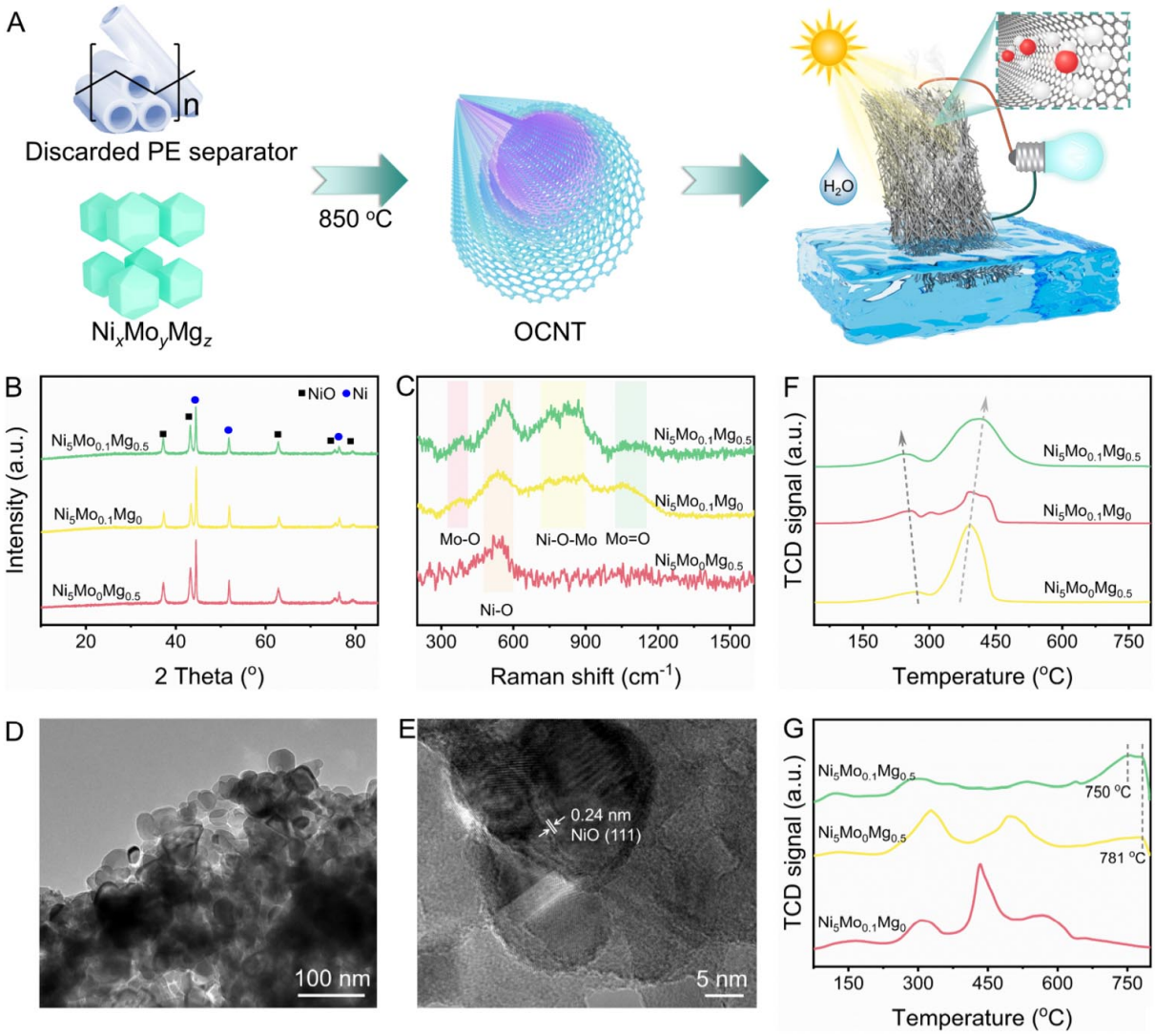

Figure 1. (A) Schematic of an OCNT evaporator from discarded PE separators for interfacial solar-driven steam and power cogeneration. (B) X-ray diffraction (XRD) profiles and (C) Raman spectra of different catalysts. (D and E) HRTEM images of $Ni_5Mo_{0.1}Mg_{0.5}$. (F) H_2-temperature programmed reduction (H_2-TPR) and (G) CO_2-temperature programmed desorption (CO_2-TPD) curves of different catalysts.

In this work, we design a multi-component nickel (Ni)-based catalyst ($Ni_xMo_yMg_z$) to convert discarded polyethylene (PE) separators into CNTs and then construct CNT dual-functional evaporators for freshwater and electricity co-generation [Figure 1A]. As the catalytic activity center in $Ni_xMo_yMg_z$, the Ni component mainly affects the carbonization reaction rate and the morphology of the carbon product. Mo effectively enhances the reducibility of NiO and prevents the sintering of Ni particles at high temperature. MgO prevents carbon deposition and improves CNT yield. Benefiting from good photo-to-thermal conversion capability, excellent hydrophilicity, and abundant oxygen-containing functional groups, the CNT evaporator achieves an evaporation rate of 2.73 kg m^{-2} h^{-1}, a photothermal efficiency of 95.4%, and an open-circuit voltage of 0.221 V. Molecular dynamics (MD) simulation reveals the mechanism of electricity generation. The oxygen-containing functional groups on the CNT surface dissociate upon contact with water molecules, generating surface charge. With continuous water evaporation, H_3O^+ is attracted by surface functional groups and follows the water flow to the evaporation end of the device, thereby establishing a potential difference between the upper and lower ends of the device.

EXPERIMENTAL

Materials and chemicals

Discarded PE separators were provided by Zhongxing Innovative Material Technologies Co. Ltd. [Supplementary Figure 1]. $Mg(NO_3)_2·6H_2O$ and $Ni(NO_3)_2·6H_2O$ were supplied by Shanghai Aladdin Biochemical Technology Co. Ltd. Poly(ethylene glycol) (PEG-200) and $(NH_4)_6Mo_7O_{24}·4H_2O$ were purchased from Sinopharm Chemical Reagent Co. Ltd. Gelatin and glutaraldehyde were supplied by Shanghai Macklin Biochemical Co. Ltd. The non-woven cotton was procured from EAXAY.

Synthesis of $Ni_xMo_yMg_z$ catalysts and $OCNT_{x-y-z}$

$Ni_xMo_yMg_z$ catalysts (where *x*, *y*, and *z* refer to the mole ratio of Ni, Mo, and Mg) were synthesized by the combustion method. Firstly, 30.00 g $Ni(NO_3)_2·6H_2O$, 2.64 g $Mg(NO_3)_2·6H_2O$, 0.36 g $(NH_4)_6Mo_7O_{24}·4H_2O$, and 10.00 g PEG-200 were mixed and milled thoroughly and then calcined at 350 °C for 15 min in a muffle furnace to prepare $Ni_5Mo_{0.1}Mg_{0.5}$ catalysts. Other catalysts with different proportions were prepared by fixing the molar amount of Ni salt added and adjusting the amounts of Mo salt and Mg salt. The detailed amounts of metal salts are listed in Supplementary Table 1.

Discarded PE separators (5.00 g) and $Ni_xMo_yMg_z$ catalyst (0.50 g) were mixed in a crucible (30 mL) and subsequently carbonized in a muffle furnace to afford CNT_{x-y-z} (850 °C, 4 min). Then, CNT_{x-y-z} was refluxed in concentrated HNO_3 at 60 °C to produce oxidized CNTs (denoted as $OCNT_{x-y-z}$).

Preparation of $OCNT_{x-y-z}$ evaporators

Firstly, $OCNT_{x-y-z}$ (20.5 mg) was added to the gelatin solution (2 wt%, 460 μL) and stirred overnight at room temperature (ca. 25 °C, 12 h, 400 rpm). Then, the mixture was spread onto cotton cloth (6.15 cm^2) and dried in air. $OCNT_{x-y-z}$ evaporators used in the indoor water evaporation experiments were prepared after soaking and crosslinking with aqueous glutaraldehyde solution (5 wt%). For comparison, a modified cotton evaporator without $OCNT_{x-y-z}$ was constructed using the same process. To meet the requirements of various scenarios, evaporators with different scales were fabricated using the same preparation process. The specific material quantities were listed in Supplementary Table 2.

Interfacial solar-driven water evaporation

An experimental system was constructed to simulate solar interfacial evaporation, including a sunlight simulator (Perfectlight, PLS-SEX300, China) and an analytical balance (Sunny Hengping Instrument, JA1003L, China) to track water mass loss. The surface temperature of evaporators was monitored using an infrared camera (Dongmei, DMI220, China). The computational methods of calculating evaporation rate and photothermal efficiency were described in Supplementary Note 1.

Hydroelectric power generation

A polyethylene terephthalate (PET) substrate (15 × 5 cm^2) was ultrasonically washed in deionized water and ethanol. Subsequently, an $OCNT_{x-y-z}$ evaporator (15 cm^2) was placed on the PET substrate and fixed with conductive adhesive as electrodes. The power generation electrodes (two L-shaped pieces) were fabricated and coated with epoxy resin. After drying at room temperature for 15 min, the encapsulated evaporation device was obtained. The generated voltage and current were monitored using a Source Measure Unit.

Characterization

A high-resolution transmission electron microscope (HRTEM, FEI, Tecnai G2 F30, Netherlands) was used to investigate the microstructure of the materials. Other characterizations were described in Supplementary Note 2.

RESULTS AND DISCUSSION

Fabrication of $Ni_xMo_yMg_z$ catalysts and $OCNT_{x-y-z}$

$Ni_xMo_yMg_z$ catalysts were produced through the combustion method [Supplementary Figure 2]. As shown in Figure 1B, the NiO diffraction peaks at 2θ = 37.3°, 43.3°, 62.9°, 75.2°, and 79.6° are assigned to the (111), (200), (220), (311), and (222) planes, respectively. Peaks attributable to Ni appear at 2θ = 44.7° (111), 51.8° (200), and 76.3° (220). Interestingly, the diffraction intensities of Ni and NiO are affected by the addition of Mo and Mg [Supplementary Figure 3]. Compared with Ni, the diffraction intensity of NiO increases with an increase in the Mo/Ni mole ratio from 0 to 0.1/5; correspondingly, the yield of $CNT_{5-y-0.5}$ rises from 11.7 to 57.4 wt% [Supplementary Figure 4A]. Mo can effectively prevent sintering and improve the dispersion of Ni particles at high temperatures, thereby making more catalytically active sites accessible[38]. As the Mo/Ni mole ration increases to 1/5, the yield of $CNT_{5-y-0.5}$ decreases sharply to 27.4 wt%. The strong interfacial interaction between metal and support promotes the generation of an inert phase that covers active sites[39], resulting in the decrease of catalyst activity. Similarly, the yield of $CNT_{5-0.1-z}$ increases first from 53.4 to 57.4 wt% (with the Mg/Ni mole ratio increasing from 0.1/5 to 0.5/5) and then decreases to 48.6 wt% (with the Mg/Ni mole ratio increasing from 0.5/5 to 2/5, Supplementary Figure 4B). However, no CNTs are produced when the Mg/Ni mole ratio is 0/5. During the carbonization process, catalyst activity is readily reduced because active sites are covered by deposited carbon. As an alkaline oxide, MgO in the composite catalyst prevents carbon deposition on the catalyst surface and improves the yield of CNT[40]. As a result, the highest carbon yield reaches 57.4 wt% when the Ni/Mo/Mg mole ratio is adjusted to 5/0.1/0.5. $Ni_5Mo_{0.1}Mg_{0.5}$ possesses higher catalytic activity than other catalysts, which is inseparable from the synergistic effect of Mo and Mg. Raman spectroscopy reveals Mo-O, Ni-O, Ni-O-Mo, and Mo=O bonds within $Ni_5Mo_{0.1}Mg_{0.5}$ [Figure 1C]. However, the first-order vibration peak of MgO is absent in the Raman spectrum due to its own lattice symmetry[41]. The morphology of $Ni_5Mo_{0.1}Mg_{0.5}$ consists of irregular clusters composed of nanoparticles with a size of 10-30 nm [Figure 1D, Supplementary Figures 5 and 6]. NiO crystal particles in $Ni_5Mo_{0.1}Mg_{0.5}$ are wrapped by amorphous MgO [Figure 1E]. The mass loss of $Ni_5Mo_{0.1}Mg_{0.5}$ at 800 °C is ca. 1.5% [Supplementary Figure 7], indicating its high thermal stability.

The effects of Mo and Mg on the overall performance of catalysts were studied using H_2-TPR and CO_2-TPD. The two reduction peaks of the H_2-TPR profile are observed at 200-300 and 300-500 °C [Figure 1F]. After the addition of Mo to the catalysts, the reduction peaks of $Ni_5Mo_{0.1}Mg_0$ and $Ni_5Mo_{0.1}Mg_{0.5}$ catalysts within 200-300 °C shift to the low-temperature region, indicating that their reducibility is stronger than that of $Ni_5Mo_0Mg_{0.5}$. Mo promotes the formation of smaller NiO clusters, thereby exposing more active sites on the catalyst[42]. Furthermore, the reduction peaks at 300-500 °C shift to higher temperatures, implying a robust interaction between Mo and Ni. A wider temperature range was observed in the $Ni_5Mo_{0.1}Mg_{0.5}$ profile because mixed-metal clusters with stronger interactions formed after the Mg addition. The characteristic peaks at low CO_2 desorption temperatures represent the weakly alkaline adsorption sites on the Ni-O-support, while the peaks at high temperatures correspond to the strongly alkaline sites. Different from $Ni_5Mo_{0.1}Mg_0$, high-temperature CO_2 desorption peaks appear at 700-800 °C for $Ni_5Mo_0Mg_{0.5}$ and $Ni_5Mo_{0.1}Mg_{0.5}$ [Figure 1G], which confirms the presence of the stronger alkaline Mg-O site and the generation of strongly monodentate carbonate[43]. Previous work showed that strong adsorption is beneficial for the efficient elimination of carbon deposition by strong basic sites (O^{2-})[44].

The morphology of carbon products is significantly affected by the mole ratio of Ni/Mo/Mg [Figure 2A]. CNT_{x-y-z} was oxidized using concentrated HNO_3 to prepare $OCNT_{x-y-z}$ with enhanced hydrophilicity. By using $Ni_5Mo_{0.1}Mg_0$ as a catalyst, the carbon product ($OCNT_{5-0.1-0}$) is composed of agglomerated spherical carbon with a size of 50-200 nm [Figure 2B, Supplementary Figure 8]. By contrast, the addition of Mg to the catalyst results in CNT formation, implying that MgO in the catalyst plays a crucial role in suppressing carbon deposition and promoting CNT growth. When the Mg/Ni mole ratio increases to 2/5, the diameter of CNT

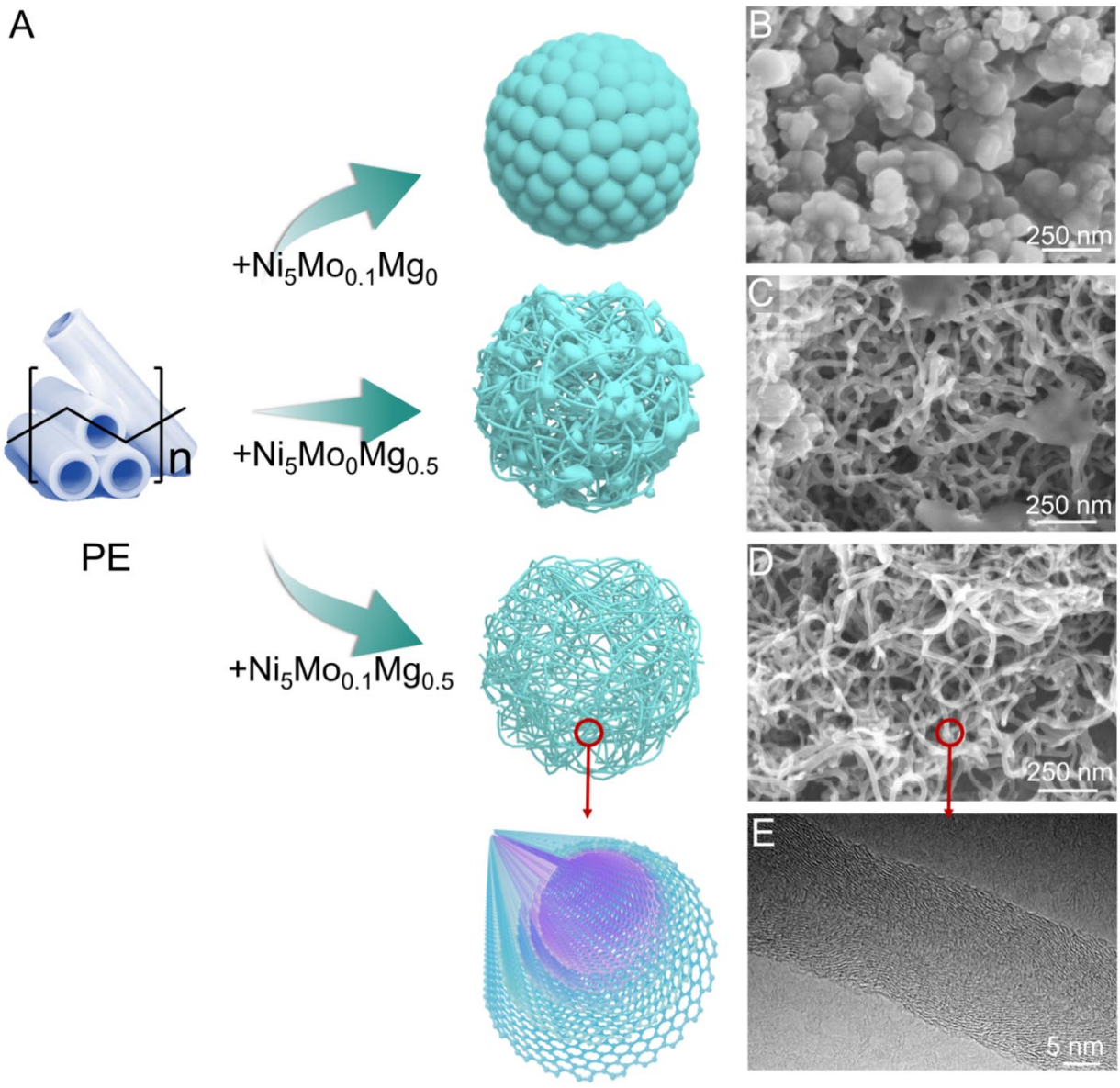

Figure 2. (A) Schematic illustration and (B-D) scanning electron microscopy (SEM) micrographs of $OCNT_{5\text{-}0.1\text{-}0}$, $OCNT_{5\text{-}0\text{-}0.5}$ and $OCNT_{5\text{-}0.1\text{-}0.5}$, and (E) HRTEM image of $OCNT_{5\text{-}0.1\text{-}0.5}$.

becomes significantly wider, and the yield of CNT decreases [Supplementary Figure 9]. By using $Ni_5Mo_0Mg_{0.5}$ as a catalyst, the $OCNT_{5\text{-}0\text{-}0.5}$ consists of amorphous carbon and a few CNTs with a length of ca. 1-5 μm [Figure 2C, Supplementary Figure 10]. However, the yield of $CNT_{5\text{-}0\text{-}0.5}$ is only 11.7 wt%, reflecting the poor catalytic activity of $Ni_5Mo_0Mg_{0.5}$. When the Mo/Ni mole ratio increases to 0.1/5, $OCNT_{5\text{-}0.1\text{-}0.5}$ features a diameter of 20-30 nm and a length of 10-30 μm [Figure 2D and E, Supplementary Figures 11 and 12], and the yield of $CNT_{5\text{-}0.1\text{-}0.5}$ is the highest. The interlayer spacing of $OCNT_{5\text{-}0.1\text{-}0.5}$ is 0.34 nm, consistent with the interlayer spacing of graphite[45]. The diameter of $OCNT_{5\text{-}0.1\text{-}0.5}$ is smaller than that of $OCNT_{5\text{-}0\text{-}0.5}$, which is attributed to the addition of the Mo element. In addition to enhancing catalyst activity, Mo effectively regulates the morphology of OCNT. As the Mo/Ni mole ratio increases to 1/5, $OCNT_{5\text{-}1\text{-}0.5}$ shows a smaller diameter and longer length than $OCNT_{5\text{-}0.1\text{-}0.5}$, but a large number of nano-carbon particles are formed [Supplementary Figure 13]. The above results prove that the appropriate addition of Mo and Mg synergistically enhances the yield and quality of CNT.

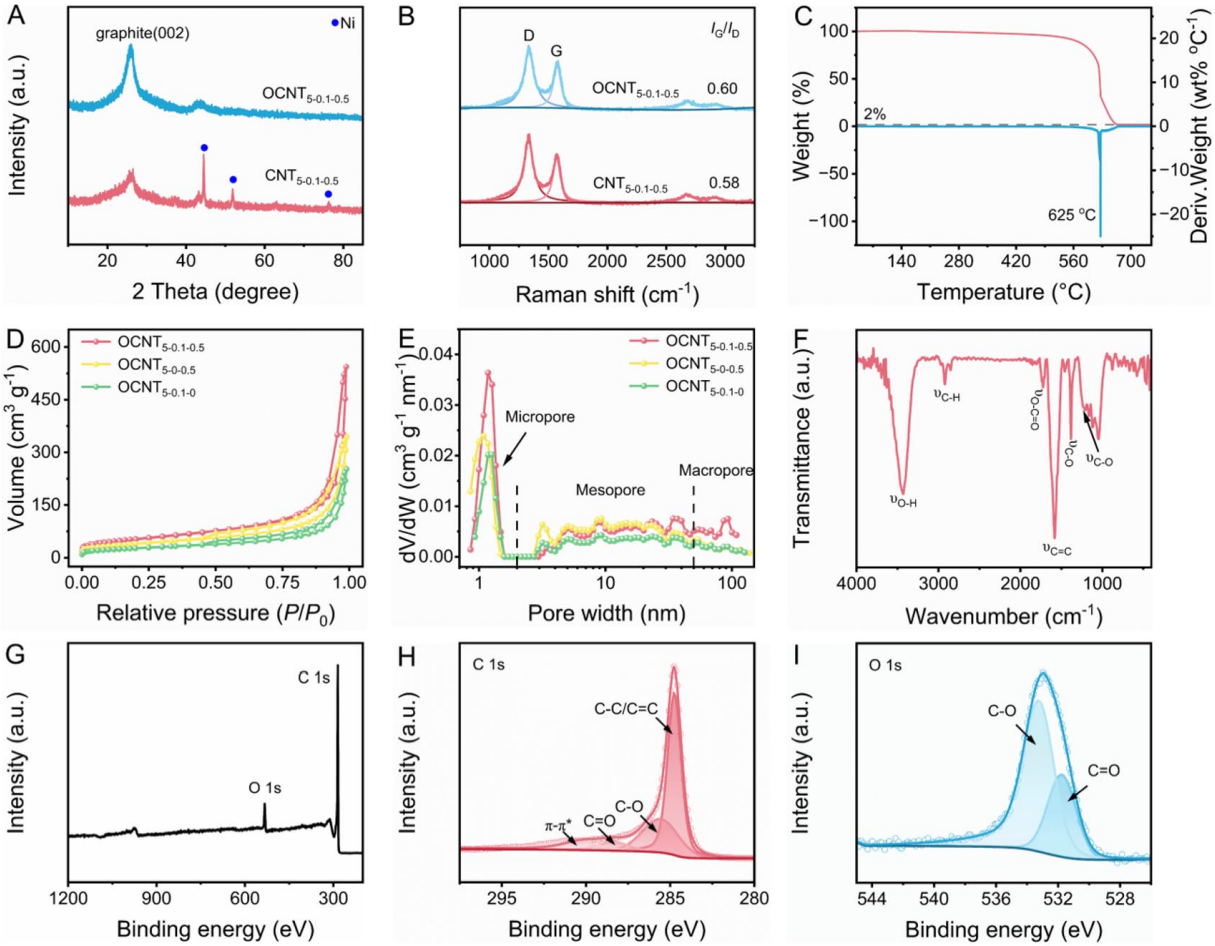

Figure 3. (A) XRD profiles and (B) Raman patterns of $OCNT_{5\text{-}0.1\text{-}0.5}$ and $CNT_{5\text{-}0.1\text{-}0.5}$. (C) Thermal gravimetric analysis (TGA) and derivative thermogravimetry (DTG) curves of $OCNT_{5\text{-}0.1\text{-}0.5}$. (D) N_2 adsorption-desorption isotherms and (E) corresponding pore size distribution using the density functional theory (DFT) model of OCNT. (F) Fourier transform infrared spectroscopy (FT-IR), (G) X-ray photoelectron spectroscopy (XPS), high-resolution (H) C 1s, and (I) O 1s XPS spectra of $OCNT_{5\text{-}0.1\text{-}0.5}$.

The phase structure of $OCNT_{5\text{-}0.1\text{-}0.5}$ was analyzed by X-ray diffraction (XRD) and Raman spectroscopy. A sharp graphite peak (002) in the XRD patterns appears at 2θ=26.5° [Figure 3A, Supplementary Figure 14A], proving the highly graphitized structure. After purification, the diffraction peak of Ni disappears, and the degree of graphitization is slightly enhanced. By fitting and calculating the peak area ratio between the D and G peaks, the I_G/I_D value of $OCNT_{5\text{-}0.1\text{-}0.5}$ is determined to be 0.60 [Figure 3B, Supplementary Figure 14B], indicating the presence of edge-unsaturated carbons, asymmetric carbon species, and/or sidewall lattice defects[46]. The thermal stability of $OCNT_{5\text{-}0.1\text{-}0.5}$ is studied by Thermal gravimetric analysis (TGA) and derivative thermogravimetry (DTG) curves. The maximum weight-loss rate occurs at 625 °C, and the weight loss after complete oxidation decomposition is 98% [Figure 3C], indicating good thermal stability and high purity. The specific surface area of $OCNT_{5\text{-}0.1\text{-}0.5}$ is 190.1 $m^2\ g^{-1}$ [Figure 3D and E], higher than that of $OCNT_{5\text{-}0.1\text{-}0}$ (95.6 $m^2\ g^{-1}$) or $OCNT_{5\text{-}0\text{-}0.5}$ (141.2 $m^2\ g^{-1}$). $OCNT_{5\text{-}1\text{-}0.5}$ exhibits a specific surface area of 167.18 $m^2\ g^{-1}$, whereas that of $OCNT_{5\text{-}0.1\text{-}2}$ reaches 191.0 $m^2\ g^{-1}$ [Supplementary Figure 15]. Furthermore, the surface elements and functional groups of $OCNT_{5\text{-}0.1\text{-}0.5}$ were analyzed using Fourier transform infrared spectroscopy (FT-IR) and X-ray photoelectron spectroscopy (XPS). As illustrated in Figure 3F, the peaks near 1,723, 1,582, and 1,383 cm^{-1} are attributed to C=O, C=C-C (aryl group), and C-O, respectively. Figure 3G reveals that carbon and oxygen are detected on the $OCNT_{5\text{-}0.1\text{-}0.5}$ surface. The curve-fitting of the high-resolution C 1s XPS spectrum reveals four peaks at 284.7, 285.6, 288.5, and 290.5 eV, corresponding to C-C/C=C, C-O, C=O, and π-π* transitions, respectively [Figure 3H]. The high-resolution O 1s XPS spectrum is decomposed into two peaks located at 531.8 and 533.2 eV [Figure 3I], attributable to C=O and C-O,

respectively.

A variety of methods have been reported for converting waste polyolefins into CNTs, for instance, chemical vapor deposition[47], Joule flash heating method[11], microwave-assisted carbonization[9,12,13], and combined catalyst carbonization[14]. Compared with these methods, the "all-in-one" catalytic strategy in this work possesses the following advantages. Firstly, the catalytic performance of Ni is synergistically enhanced by the addition of Mo and Mg, thereby enabling the controlled growth of CNTs from a single catalyst without additional degradation catalysts. Secondly, CNTs are directly prepared in a few minutes under ambient air without any protective gas. Finally, the catalytic method shows potential for large-scale CNT preparation.

Photothermal properties of $OCNT_{x\text{-}y\text{-}z}$ evaporators

The $OCNT_{5\text{-}0.1\text{-}0.5}$ evaporator is constructed by coating the dispersion of $OCNT_{5\text{-}0.1\text{-}0.5}$ and gelatin on cotton cloth, followed by crosslinking with glutaraldehyde [Figure 4A]. $OCNT_{5\text{-}0.1\text{-}0.5}$ is evenly distributed on the surface of the evaporator [Figure 4B and C, Supplementary Figure 16]. Similarly, $OCNT_{5\text{-}0.1\text{-}0}$ and $OCNT_{5\text{-}0\text{-}0.5}$ evaporators are prepared [Supplementary Figures 17 and 18]. The optical absorption performance of the evaporators was characterized by a UV-Vis-NIR absorption spectrum. The $OCNT_{5\text{-}0.1\text{-}0.5}$ evaporator exhibits an average light absorption of 98% within a broadband spectral range of 300-2500 nm [Figure 4D], greater than that of the cotton evaporator (ca. 48%). The absorptions of $OCNT_{5\text{-}0\text{-}0.5}$ and $OCNT_{5\text{-}0.1\text{-}0}$ evaporators reached 97% and 95%, respectively [Supplementary Figure 19A]. Due to high light absorption, the surface temperature of the $OCNT_{5\text{-}0.1\text{-}0.5}$ evaporator increased rapidly to 94.2 °C after irradiation of 1 Sun for 2 min [Figure 4E and F], reflecting dramatic photothermal conversion ability. Under 1 Sun illumination for 15 min, the surface temperature of the cotton evaporator reaches only 44 °C. For $OCNT_{5\text{-}0.1\text{-}0}$ and $OCNT_{5\text{-}0\text{-}0.5}$ evaporators, the temperature was stable at ca. 94 and 96 °C under irradiation of 1 Sun, respectively [Supplementary Figures 19B and 20]. The hydrophilicity of evaporators is evaluated by water contact angle. It takes 84 s for a water droplet to completely wet the cotton evaporator. The contact angle of the $OCNT_{5\text{-}0.1\text{-}0.5}$ evaporator decreases rapidly to 0° within 0.03 s [Supplementary Video 1], while $OCNT_{5\text{-}0.1\text{-}0}$ and $OCNT_{5\text{-}0\text{-}0.5}$ evaporators require 3 and 0.03 s, respectively [Figure 4G, Supplementary Figure 21]. The hydrophilic property is inseparable from rich oxygen-containing functional groups and large amounts of pore channels, which improve water transport capacity during evaporation.

Solar interfacial steam-power cogeneration using $OCNT_{x\text{-}y\text{-}z}$ evaporators

A self-built evaporation device was established for solar interfacial steam generation, as shown in Figure 5A and Supplementary Figure 22. A polystyrene (PS) foam serves as a supporting and thermal isolation material to prevent heat loss and transfer. Based on the good photothermal conversion ability and hydrophilicity of the $OCNT_{5\text{-}0.1\text{-}0.5}$ evaporator, water rapidly transfers to its surface to complete evaporation (from liquid to gas). For all evaporation systems, water mass loss increases linearly with irradiation time [Figure 5B]. The evaporation rate of the $OCNT_{5\text{-}0.1\text{-}0.5}$ evaporator is 2.73 kg m^{-2} h^{-1} [Figure 5C], higher than that of the $OCNT_{5\text{-}0.1\text{-}0}$ evaporator (2.39 kg m^{-2} h^{-1}), $OCNT_{5\text{-}0\text{-}0.5}$ evaporator (2.48 kg m^{-2} h^{-1}), or cotton evaporator (0.88 kg m^{-2} h^{-1}). The $OCNT_{5\text{-}0.1\text{-}0.5}$ evaporator shows a high evaporation rate, attributed to high light absorption & photothermal conversion ability, rich pore channels & functional groups, and good thermal localization. Solar intensity is an important factor affecting the evaporation rate of evaporators. The water mass of the $OCNT_{5\text{-}0.1\text{-}0.5}$ evaporation system decreases linearly with irradiation time under different light intensities [Figure 5D]. As the light intensity is enhanced from 0.5 to 3.0 Sun, the evaporation rate increases from 1.51 to 6.99 kg m^{-2} h^{-1} [Figure 5E]. Over 10 cycles of water evaporation, the $OCNT_{5\text{-}0.1\text{-}0.5}$ evaporator exhibits an average evaporation rate of 2.71 kg m^{-2} h^{-1} [Figure 5F]. Besides, the photothermal conversion efficiency of the $OCNT_{5\text{-}0.1\text{-}0.5}$ evaporator is calculated to be 95.4%, which is superior to that of many previously reported evaporators [Figure 5G, Supplementary Table 3].

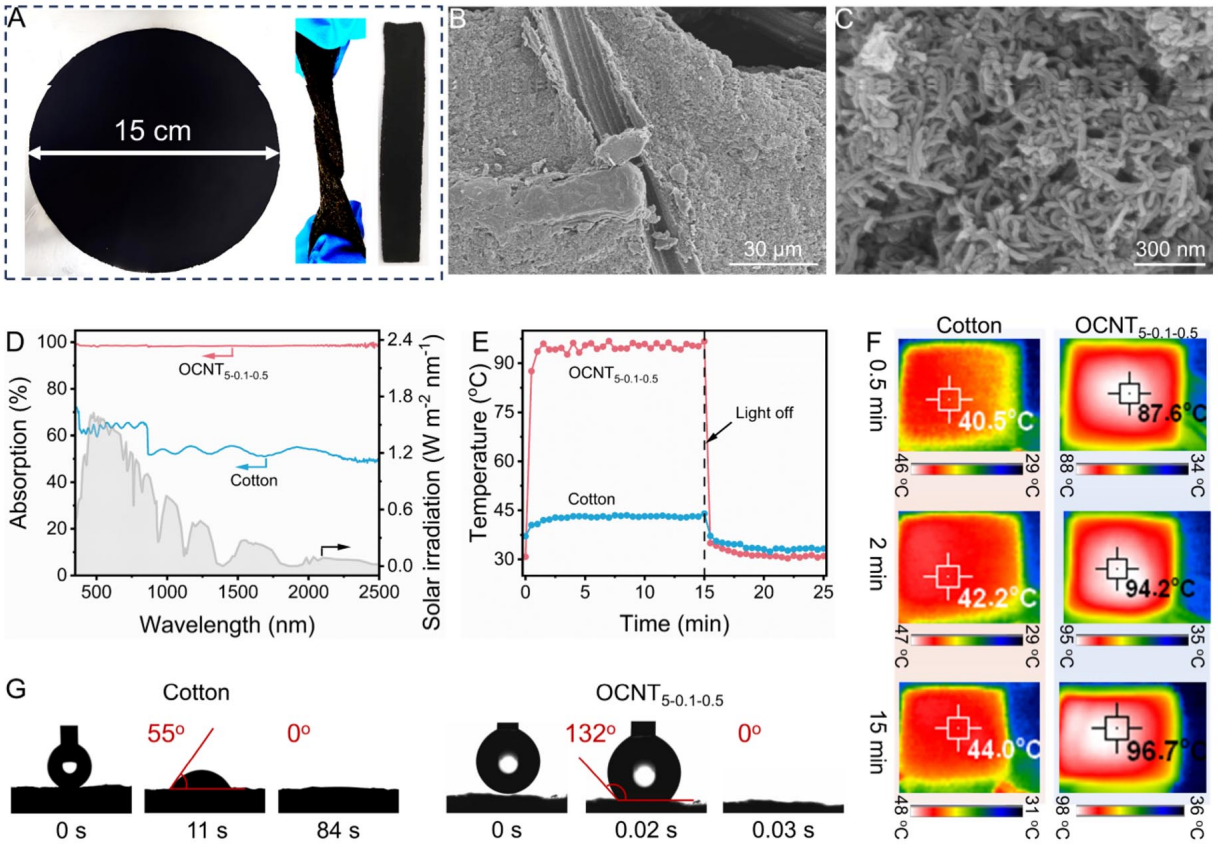

Figure 4. (A) Photographs and (B and C) SEM images of the $OCNT_{5\text{-}0.1\text{-}0.5}$ evaporator. (D) UV-Vis-NIR absorption spectra, (E) surface temperature curves, (F) infrared thermal images, and (G) water contact angles of cotton and $OCNT_{5\text{-}0.1\text{-}0.5}$ evaporators.

The evaporation performance is closely tied to the latent heat of water evaporation. Under dark conditions, the water mass losses are 426 mg for $OCNT_{5\text{-}0.1\text{-}0.5}$, 360 mg for $OCNT_{5\text{-}0.1\text{-}0}$, 375 mg for $OCNT_{5\text{-}0\text{-}0.5}$, and 306 mg for cotton, higher than that of pure water (295 mg) [Figure 5H]. Correspondingly, the evaporation enthalpies were calculated as 1.686, 1.995, 1.915, and 2.347 kJ g^{-1} [Supplementary Note 3], which are similar to those of the DSC measurement [Supplementary Figure 23 and Supplementary Table 4]. The lowest evaporation enthalpy of the $OCNT_{5\text{-}0.1\text{-}0.5}$ evaporator is the fundamental reason for its higher evaporation rate than that of other evaporators[48]. Compared with pure water, the evaporation enthalpy is reduced by 30.7% for the $OCNT_{5\text{-}0.1\text{-}0.5}$ evaporator. In addition, the thermal conductivity of the $OCNT_{5\text{-}0.1\text{-}0.5}$ evaporator is measured as 0.0752 W m^{-1} K^{-1}. The heat distribution of the evaporation system is analyzed by finite element simulation [Supplementary Note 4]. The $OCNT_{5\text{-}0.1\text{-}0.5}$ evaporator exhibits a higher surface temperature than cotton due to the good photothermal conversion ability of $OCNT_{5\text{-}0.1\text{-}0.5}$ [Figure 5I, Supplementary Figure 24]. The localization of heat on the surface of the evaporator promotes the liquid water-to-vapor conversion. The heat loss of the $OCNT_{5\text{-}0.1\text{-}0.5}$ evaporator during water evaporation is calculated as 15.7% [Supplementary Note 5].

The water-evaporation power-generation device is shown in Figure 6A. The evaporator was cut into rectangles (10 × 1.5 cm^2) to facilitate the generation of electrical energy [Supplementary Figures 25 and 26]. The electrodes at the ends of the evaporators were encapsulated with epoxy resin to prevent short circuits or oxidation, and the device was placed at 45°. The numerous oxygenated chemical groups and abundant pore channels of $OCNT_{5\text{-}0.1\text{-}0.5}$ facilitate water transport. Under the synergistic action of capillary forces and hydrophilic properties, water is continuously transported from the bottom of the evaporator to the surface. The abundant oxygen-containing functional groups of $OCNT_{5\text{-}0.1\text{-}0.5}$ dissociate and generate surface charge

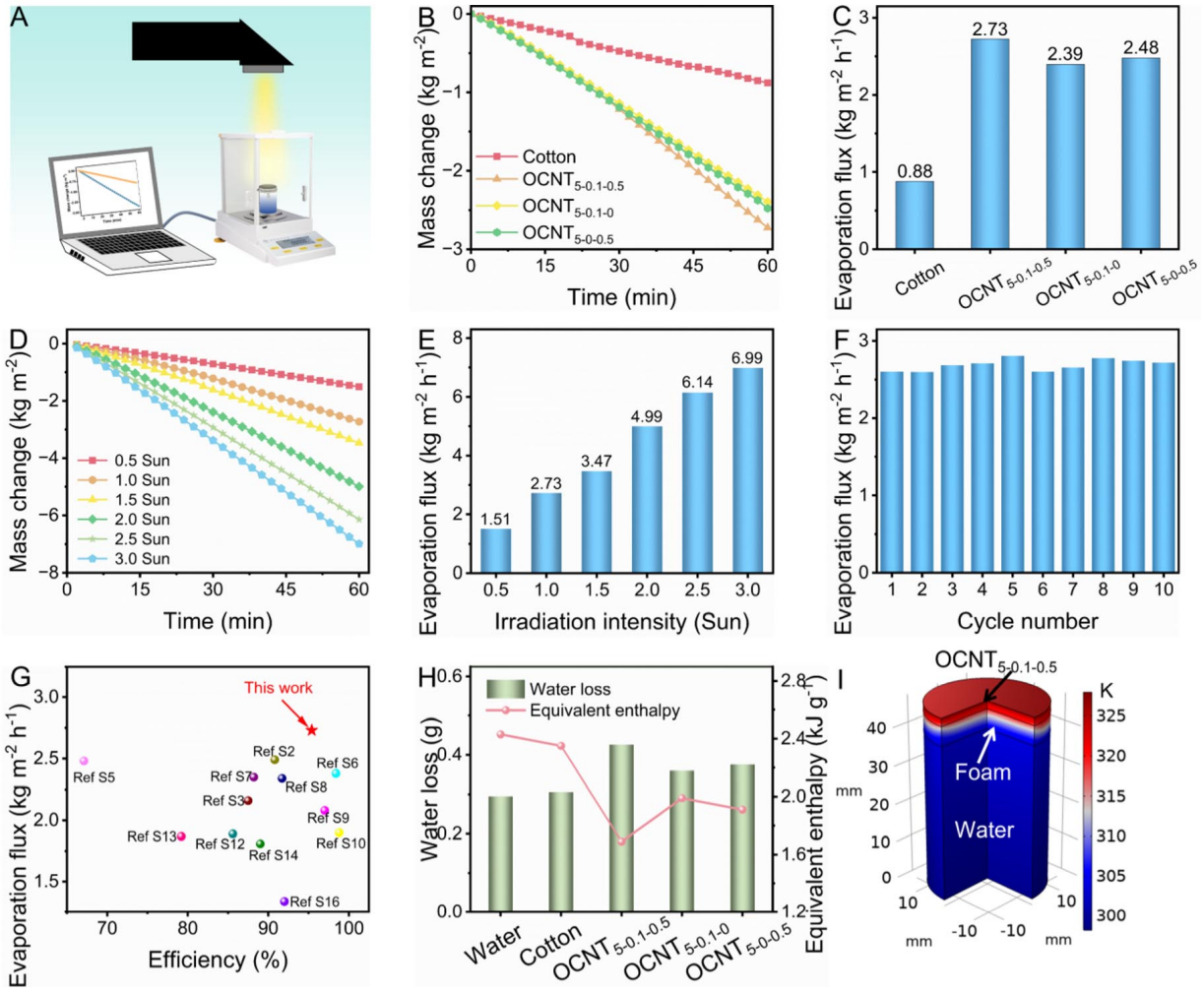

Figure 5. (A) Schematic diagram of interfacial solar steam generation. (B) Water mass losses of evaporation systems and (C) evaporation fluxes for various evaporators under 1 Sun irradiation. (D) Water mass change and (E) evaporation flux of the $OCNT_{5\text{-}0.1\text{-}0.5}$ evaporator under solar intensities ranging from 0.5 to 3 Sun. (F) Water evaporation fluxes of the $OCNT_{5\text{-}0.1\text{-}0.5}$ evaporator over 10 cycles. (G) Solar-evaporation performance comparison between the $OCNT_{5\text{-}0.1\text{-}0.5}$ evaporator and previously reported evaporators. (H) Mass loss of water in the dark and vaporization enthalpy for various evaporators. (I) COMSOL simulation of the temperature distribution in the $OCNT_{5\text{-}0.1\text{-}0.5}$ evaporation system.

upon contact with water molecules. Under the electric double-layer effect at the solid-liquid interface, the counterions selectively migrate in the nanochannels of the evaporator. The continuous enrichment of counterions at the evaporation end leads to the formation of a potential difference [Supplementary Figure 27]. When the external circuit is connected, the potential difference can drive current, producing power output. $OCNT_{5\text{-}0.1\text{-}0.5}$, $OCNT_{5\text{-}0.1\text{-}0}$, and $OCNT_{5\text{-}0\text{-}0.5}$ devices yield the maximum open-circuit voltage of 0.221, 0.130, and 0.082 V, respectively, all exceeding that of cotton [Figure 6B]. Correspondingly, the generated currents were 0.21, 0.15, and 0.11 μA, respectively [Figure 6C]. Specifically, the generated voltage was relatively stable between 0.21 and 0.18 V over 10,000 s, while the current decreased from approximately 220 to 100 nA due to the gradual variation in the evaporation-driven ion transport process [Figure 6D]. The power-generation performance of $OCNT_{5\text{-}0.1\text{-}0.5}$ devices is better than that of $OCNT_{5\text{-}0.1\text{-}0}$ and $OCNT_{5\text{-}0\text{-}0.5}$ devices, due to abundant pores, high-quality CNT structure, and abundant functional groups. The Zeta potential generated by $OCNT_{5\text{-}0.1\text{-}0.5}$, $OCNT_{5\text{-}0.1\text{-}0}$, and $OCNT_{5\text{-}0\text{-}0.5}$ in aqueous solution is -9.3, -1.16, and -6.69 mV, respectively [Figure 6E]. Compared with many reported power generation devices, the $OCNT_{5\text{-}0.1\text{-}0.5}$ device exhibits better steam and electricity co-generation performance [Figure 6F, Supplementary Table 5].

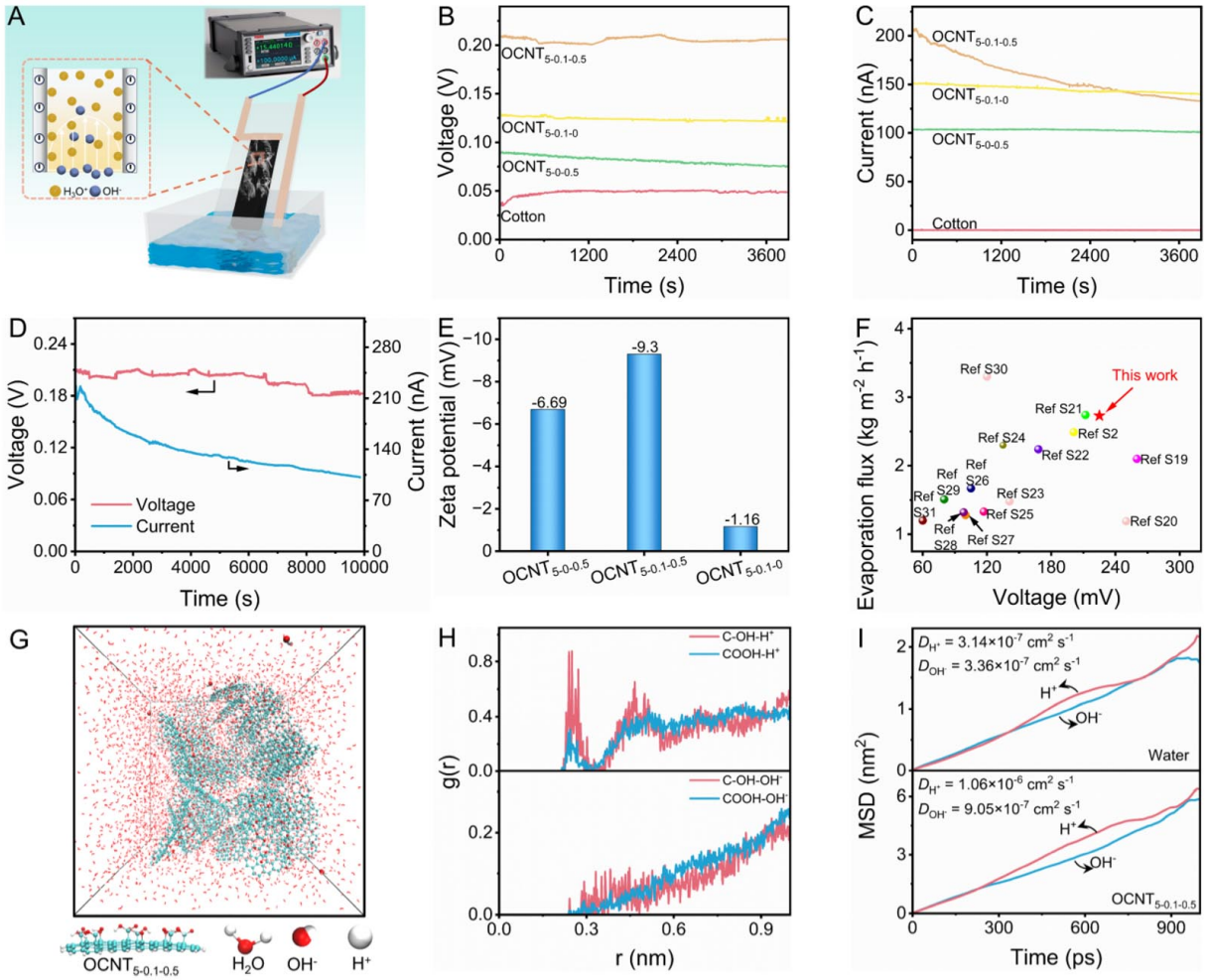

Figure 6. (A) Water evaporation electricity generation device schematic. (B) Open-circuit voltage and (C) short-circuit current generated for various devices. (D) Electricity generation curves for the $OCNT_{5\text{-}0.1\text{-}0.5}$ device after running for 10,000 s. (E) Zeta potential of $OCNT_{5\text{-}0.1\text{-}0.5}$, $OCNT_{5\text{-}0.1\text{-}0}$, and $OCNT_{5\text{-}0\text{-}0.5}$ devices. (F) Performance comparison of the $OCNT_{5\text{-}0.1\text{-}0.5}$ device with some previous devices. (G) Molecular dynamics (MD) simulation sample snapshots. (H) RDF plots of C-OH and COOH interacting with H^+ and OH^-. (I) Mean square displacement (MSD) plots for ion diffusion in pure water or $OCNT_{5\text{-}0.1\text{-}0.5}$ and pure water.

Streaming potential is commonly accepted as the primary mechanism underlying electricity generation in hydrovoltaic processes[49-52]. During spontaneous water evaporation, the aqueous electrolyte solution migrates from the bottom to the top and flows over the surface of the charged material. The counterions from the electrolyte solution are attracted by the charged ions in the nanopores of $OCNT_{5\text{-}0.1\text{-}0.5}$, resulting in the formation of an electric double layer. The potential difference between the upper and lower ends is gradually formed due to the continuous directional migration and accumulation of free charge. Actually, hydrovoltaic power generation is the process of converting environmental latent heat into electrical energy, which depends on the interaction between ions and $OCNT_{5\text{-}0.1\text{-}0.5}$ materials. Ion selectivity and charge separation in the nanochannel are usually governed by the ion-functional-group interactions, which are further investigated using MD simulation [Supplementary Figure 28 and Supplementary Note 6]. H_3O^+ and OH^-, produced by the dissociation of water molecules, were added to the simulation system [Figure 6G]. To simplify the simulation, H^+ was placed in the simulation system instead of H_3O^+ in the real-world environment. The MD simulation was performed in an NPT ensemble (constant number of particles (N), pressure (P), and temperature (T)) with a simulation time of 20 ns. The relationship between the ionic charge and the surface functional groups of materials in the simulation system was analyzed using the radial distribution function (RDF). As shown in Figure 6H, the first peaks of radial distribution between H^+ and

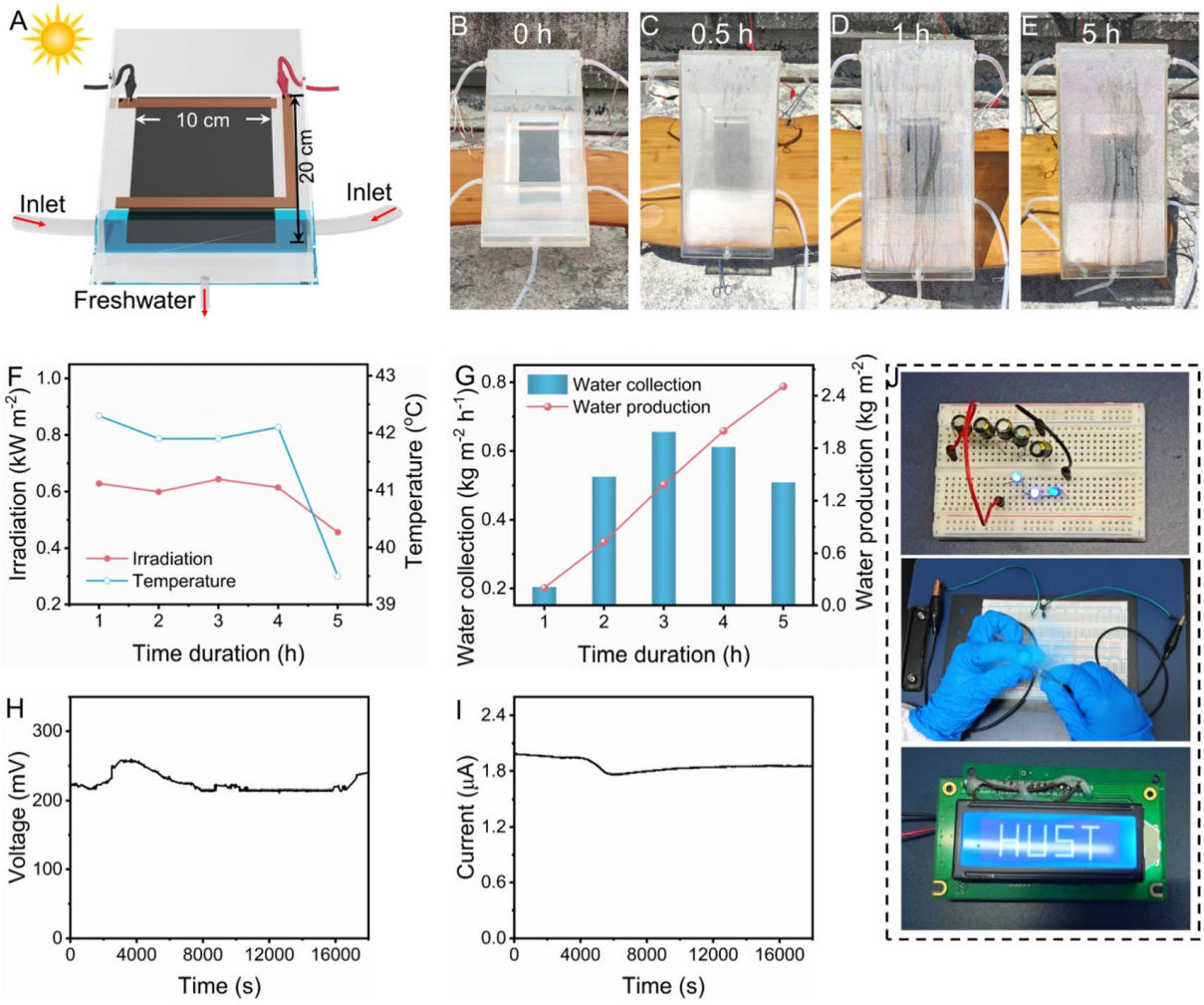

Figure 7. (A) Scheme and (B-E) photographs of the outdoor device. (F) Solar irradiation intensity and temperature, (G) water production, (H) voltage, and (I) current curves of the $OCNT_{5\text{-}0.1\text{-}0.5}$ device in the practical experiment. (J) Photographs showing low-power electrical appliances powered by series-connected capacitors.

oxygen-containing functional groups in $OCNT_{5\text{-}0.1\text{-}0.5}$ molecules appear at 0.25 nm (C-OH) and 0.238 nm (COOH), respectively. By comparison, the first peak of C-OH-H^+ is stronger than that of COOH-H^+. However, there is no obvious peak in the radial distribution between OH^- and oxygen-containing functional groups, indicating the absence of coordination. The diffusion coefficients of H^+ and OH^- are 1.06×10^{-6} and 9.05×10^{-7} cm^2 s^{-1}, respectively [Figure 6I]. In the pure water system, the diffusion coefficients are 3.14×10^{-7} and 3.36×10^{-7} cm^2 s^{-1}, respectively. The faster diffusion of H^+ after the addition of $OCNT_{5\text{-}0.1\text{-}0.5}$ confirms the strong attraction between H^+ and $OCNT_{5\text{-}0.1\text{-}0.5}$. During water evaporation, H_3O^+ selectively migrates in the nanochannels of the evaporator and accumulates at the evaporation section, resulting in the formation of a potential difference.

Outdoor solar evaporation-hydrovoltaic co-generation of $OCNT_{5\text{-}0.1\text{-}0.5}$ device

The practical freshwater-power co-generation experiment was carried out outdoors [Supplementary Figures 29 and 30]. The self-built outdoor device [Figure 7A] mainly included an evaporator, a container of bulk water, an evaporation chamber, a vapor condenser, and a freshwater collector. With continuous evaporation and bulk water consumption, water in the container can be supplied in time through inlets. The $OCNT_{5\text{-}0.1\text{-}0.5}$ evaporator (20×10 cm^2) was connected by two wires and placed in the evaporation chamber. As the sun shines, liquid water is constantly evaporated and collected, while

generating electricity [Figure 7B-E]. As the vapor condensed, the droplets slid under gravity and were collected at the outlet. The maximum temperature and radiation intensity are 42.3 °C and 0.64 kW m^{-2}, respectively [Figure 7F]. The maximum water collection rate is 0.66 kg m^{-2} h^{-1} [Figure 7G]. The water production rate is lower than that in the indoor experiment, mainly attributed to lower solar intensity (< 0.8 kW m^{-2}) and saturated vapor pressure induced by the closed system. The cumulative water production reaches 2.51 kg m^{-2} during a 5-h outdoor test. The device yields an open-circuit voltage of 0.215-0.265 V [Figure 7H] and a short-circuit current of 1.8-2.0 μA [Figure 7I]. To further demonstrate the potential utilization of the generated energy, multiple power-generation devices are connected in series/parallel configurations to generate electricity that is subsequently collected through an external circuit and stored in capacitors [Supplementary Figure 31]. Finally, low-power electrical appliances, such as an LED light bulb, fan, and display screen, are powered by connecting capacitors in series [Figure 7J, Supplementary Video 2]. The above results indicate that the $OCNT_{5\text{-}0.1\text{-}0.5}$ device possesses practical application value for co-generating freshwater and power.

CONCLUSIONS

In summary, a versatile OCNT photothermal evaporator is developed to enable the simultaneous production of freshwater and electricity under solar illumination. Particularly, a $Ni_5Mo_{0.1}Mg_{0.5}$ catalyst with high catalytic activity, dispersion, and stability is designed and prepared to convert discarded polyolefin separators into OCNT. Under the synergistic effect of Ni, Mo, and Mg, the $Ni_5Mo_{0.1}Mg_{0.5}$ catalyst exhibits high reducibility, sintering resistance, and carbon elimination ability. $CNT_{5\text{-}0.1\text{-}0.5}$ is produced with a yield of 57.4 wt%. The $OCNT_{5\text{-}0.1\text{-}0.5}$ presents a diameter of 20-30 nm, a length of 10-30 μm, and contains abundant oxygen-containing functional groups. The $OCNT_{5\text{-}0.1\text{-}0.5}$ evaporator exhibited good photo-to-thermal conversion ability, satisfying hydrophilicity, high photo-to-thermal conversion efficiency (95.4%), and minimal vaporization enthalpy (1.686 kJ g^{-1}). Consequently, an evaporation rate of 2.73 kg m^{-2} h^{-1} and a voltage output of 0.221 V are achieved. In the outdoor experiment, the total water output is 2.51 kg m^{-2} over 5 h, and the voltage and current are 0.215-0.265 V and 1.8-2.0 μA, respectively. The electricity can power an LED light bulb, fan, and display screen. MD simulations reveal that H^+ from the dissociation of water molecules interacts more strongly with the surface functional groups (C-OH and COOH) of OCNT. As a result, H^+ migrates faster in the nanochannels of the evaporator than OH^-, causing a potential difference across the two ends of the device. This work presents green strategies for upcycling discarded polyolefin separators to prepare CNT and address the shortage of freshwater and energy.

DECLARATIONS

Acknowledgments

We are grateful to the Analytical and Testing Center of HUST for access to their facilities. The authors extend their gratitude to the Theoretical and Computational Chemistry Team (from Scientific Compass www.shiyanjia.com) for providing invaluable assistance.

Authors' contributions

Conceptualization, data curation, writing and manuscript revision: Gong, J.; Wang, H.; Niu, R.
Experimentation, methodology, formal analysis: Wang, H.; Xu, M.; Wen, X.; Hu, G.; Wei, Q.
Performed the simulations: Wang, H.; Feng, L.; Zhang, X.
All authors contributed to the discussion of the manuscript.

Availability of data and materials

The data supporting the findings of this study are available within this Article and its Supplementary Materials. Further data are available from the corresponding author upon request.

AI and AI-assisted tools statement

Not applicable.

Financial support and sponsorship

The present work is supported by the National Natural Science Foundation of China (No. 52373099).

Conflicts of interest

All authors declared that there are no conflicts of interest.

Ethical approval and consent to participate

Not applicable.

Consent for publication

Not applicable.

Supplementary Materials

Supplementary Materials

REFERENCES

1. Wu, S.; Huang, C.; Shen, W.; et al. A water-soluble binder for recyclable lithium-ion batteries. *Nat. Sustain.* **2026**, *9*, 575-84. DOI
2. Huang, Y. Sensing systems for safe lithium-ion batteries. *Nat. Electron.* **2025**, *8*, 452. DOI
3. Liu, Q.; Yu, Z.; Hu, Y.; Tang, M.; Zhang, Q.; Ye, M. Designing advanced separators toward lithium-ion batteries. *Adv. Energy. Mater.* **2025**, *15*, e03217. DOI
4. Arora, P.; Zhang, Z. Battery separators. *Chem. Rev.* **2004**, *104*, 4419-62. DOI PubMed
5. Sun, J.; Dong, J.; Gao, L.; Zhao, Y.; Moon, H.; Scott, S. L. Catalytic upcycling of polyolefins. *Chem. Rev.* **2024**, *124*, 9457-579. DOI PubMed PMC
6. Conk, R. J.; Stahler, J. F.; Shi, J. X.; et al. Polyolefin waste to light olefins with ethylene and base-metal heterogeneous catalysts. *Science* **2024**, *385*, 1322-7. DOI
7. Li, H.; Wu, J.; Jiang, Z.; et al. Hydroformylation of pyrolysis oils to aldehydes and alcohols from polyolefin waste. *Science* **2023**, *381*, 660-6. DOI
8. Ren, S.; Xu, X.; Hu, K.; et al. Salt-templated transformation of waste plastics into single-atom catalysts for environmental and energy applications. *Nat. Commun.* **2025**, *16*, 8194. DOI
9. Jie, X.; Li, W.; Slocombe, D.; et al. Microwave-initiated catalytic deconstruction of plastic waste into hydrogen and high-value carbons. *Nat. Catal.* **2020**, *3*, 902-12. DOI
10. Zhang, S.; Sun, N.; Li, X.; Soomro, R. A.; Xu, B. Closed pore engineering of activated carbon enabled by waste mask for superior sodium storage. *Energy. Storage. Mater.* **2024**, *66*, 103183. DOI
11. Wyss, K. M.; Li, J. T.; Advincula, P. A.; et al. Upcycling of waste plastic into hybrid carbon nanomaterials. *Adv. Mater.* **2023**, *35*, 2209621. DOI
12. Irfan, M.; Saleem, R.; Shoukat, B.; et al. Production of combustible fuels and carbon nanotubes from plastic wastes using an in-situ catalytic microwave pyrolysis process. *Sci. Rep.* **2023**, *13*, 9057. DOI PubMed PMC
13. Qiao, Y.; Chen, X.; Wang, Z.; Xu, W.; Gan, Z.; Wang, J. Microwave-assisted catalytic upcycling of polyolefin wastes into hydrogen and carbon nanotubes over Pt-promoted Fe/Ni bimetallic catalysts. *Appl. Catal. B. Environ. Energy.* **2026**, *384*, 126214. DOI
14. Wei, Q.; Hu, G.; Wang, H.; et al. When waste plastics meet with MOF: upcycling waste polypropylene separator into carbon nanotube for efficient freshwater and hydroelectricity co-generation. *Sustain. Mater. Technol.* **2026**, *47*, e01785. DOI
15. Wu, Q.; Lv, X.; Xu, N.; et al. Upcycling plastic polymers into single-walled carbon nanotubes from a magnesia supported iron catalyst. *Carbon* **2023**, *215*, 118492. DOI
16. He, S.; Li, C.; Sun, H.; et al. Promotion of manganese on Fe-based catalyst for the production of carbon nanotubes (CNTs) from plastics. *Chem. Eng. J.* **2024**, *492*, 152306. DOI
17. Zhao, J.; Gao, J.; Wang, D.; et al. Microwave-intensified catalytic upcycling of plastic waste into hydrogen and carbon nanotubes over self-dispersing bimetallic catalysts. *Chem. Eng. J.* **2024**, *483*, 149270. DOI
18. Dong, C.; Chen, L.; Lin, W.; et al. Nature-inspired 3D hierarchical carbon nanotube matrices enable extraordinary solar steam generation. *Carbon. Energy.* **2025**, *7*, e655. DOI
19. Li, Y.; Shi, Y.; Wang, H.; et al. Recent advances in carbon-based materials for solar-driven interfacial photothermal conversion water evaporation: assemblies, structures, applications, and prospective. *Carbon. Energy.* **2023**, *5*, e331. DOI

20. Zhang, Q.; Xiao, X.; Zhao, G.; et al. An all-in-one and scalable carbon fibre-based evaporator by using the weaving craft for high-efficiency and stable solar desalination. *J. Mater. Chem. A.* **2021**, *9*, 10945-52. DOI
21. Sun, J.; Farid, M. U.; Xi, W.; et al. Hydrogel-based photothermal-catalytic membrane for efficient cogeneration of freshwater and hydrogen in membrane distillation system. *Adv. Funct. Mater.* **2025**, *36*, 2416768. DOI
22. Wei, D.; Wang, C.; Zhang, J.; et al. Water activation in solar-powered vapor generation. *Adv. Mater.* **2023**, *35*, 2212100. DOI
23. Dang, C.; Cao, Y.; Nie, H.; et al. Structure integration and architecture of solar-driven interfacial desalination from miniaturization designs to industrial applications. *Nat. Water.* **2024**, *2*, 115-26. DOI
24. Opoku, K. N.; Wei, Y.; Dankwa, C. A. A.; et al. Advances in photothermal water evaporation: synthesis, mechanisms, and coupled techniques. *Energy. Mater.* **2025**, *5*, 500020. DOI
25. Mao, Z.; Chen, X.; Chen, Y.; et al. A hierarchical salt-rejection strategy for sustainable and high-efficiency solar-driven desalination. *Nano. Mater. Sci.* **2024**, *6*, 38-43. DOI
26. Liu, M.; Sun, Y.; Shao, K.; et al. Synergistic solar-powered water-electricity generation: an integrated floating system on water. *Nano. Energy.* **2024**, *119*, 109074. DOI
27. Wang, W.; Shi, Y.; Zhang, C.; et al. Conversion and storage of solar energy for cooling. *Energy. Environ. Sci.* **2022**, *15*, 136-45. DOI
28. Wang, J.; Sun, M.; Liu, C.; et al. Customized microenvironments spontaneously facilitate coupled engineering of real-life large-scale clean water capture and pollution remediation. *Adv. Mater.* **2023**, *35*, 2306103. DOI
29. Li, Z.; Zhang, J.; Zhang, J.; et al. Solar evaporator coupled with strong/weak convection and its cascade utilization. *Sci. Bull.* **2025**, *70*, 1264-74. DOI
30. Huang, W.; Gao, X.; Sun, L.; et al. Black g-C_3N_4-based hydrogel for water evaporation and photothermal persulfate activation. *J. Mater. Sci. Technol.* **2026**, *249*, 153-63. DOI
31. Li, N.; Zhang, X.; Zhu, J.; Xiong, S.; Xu, Y.; Li, Y. Bioinspired flexible composite hydrogels for efficient solar steam generation and stable electricity harvest. *Nano. Lett.* **2025**, *25*, 10072-81. DOI
32. Zhang, X.; Guo, J.; Zou, Z.; et al. Bioinspired and 3D-printed solar evaporators for highly efficient freshwater-electricity co-generation. *Mater. Horiz.* **2025**, *12*, 5211-24. DOI
33. Wang, F.; Zhang, Y.; Shi, J.; et al. Bioinspired and biodegradable functionalized graphene oxide/deacetylated cellulose acetate composite janus membranes for water evaporation-induced electricity generation. *ACS. Sustain. Chem. Eng.* **2023**, *11*, 9792-803. DOI
34. Ma, J.; Guo, Z.; Han, X.; et al. Reduced graphene oxide/FeOOH-based asymmetric evaporator for the simultaneous generation of clean water and electrical power. *Carbon* **2023**, *201*, 318-27. DOI
35. Hu, G.; Liu, H.; Liu, K.; et al. All-in-one carbon foam evaporators for efficient co-generation of freshwater and electricity. *Adv. Funct. Mater.* **2025**, *35*, 2423781. DOI
36. Ding, Y.; Li, S.; Tian, J.; et al. CNTs/Wood composite nanogenerator for producing both steam and electricity. *ACS. Appl. Electron. Mater.* **2021**, *3*, 5287-95. DOI
37. Wu, Y.; Ma, J.; Zang, S.; et al. Multifunctional composite membranes for interfacial solar steam and electricity generation. *Chem. Eng. J.* **2023**, *472*, 144600. DOI
38. Aboul-enein, A. A.; Awadallah, A. E. Production of nanostructured carbon materials using Fe-Mo/MgO catalysts via mild catalytic pyrolysis of polyethylene waste. *Chem. Eng. J.* **2018**, *354*, 802-16. DOI
39. Beck, A.; Huang, X.; Artiglia, L.; et al. The dynamics of overlayer formation on catalyst nanoparticles and strong metal-support interaction. *Nat. Commun.* **2020**, *11*, 3220. DOI PubMed PMC
40. Sattari, O.; Nematollahi, B.; Rezaei, M.; Alavi, S. M. Effect of MgO on the catalytic activity and stability of nickel-based catalyst in methane dry reforming reaction. *Sci. Rep.* **2025**, *15*, 39649. DOI PubMed PMC
41. Dekermenjian, M.; Ruediger, A. P.; Merlen, A. Raman spectroscopy investigation of magnesium oxide nanoparticles. *RSC. Adv.* **2023**, *13*, 26683-9. DOI PubMed PMC
42. Lu, J.; Veksha, A.; Lisak, G. Conversion of municipal sewage sludge into biogenic multi-walled carbon nanotubes and hydrogen using X-Mo/MgO (X = Co, Fe, Ni) catalysts through pyrolysis-chemical vapor deposition process. *Chem. Eng. J.* **2024**, *496*, 153794. DOI
43. Gao, W.; Zhou, T.; Wang, Q. Controlled synthesis of MgO with diverse basic sites and its CO_2 capture mechanism under different adsorption conditions. *Chem. Eng. J.* **2018**, *336*, 710-20. DOI
44. Xue, Q.; Li, Z.; Yi, H.; et al. Controlling sintering and carbon deposition with post-coated MgO confined group VIII metal-based catalysts towards durable high-temperature steam reforming. *Appl. Catal. B. Environ.* **2022**, *318*, 121874. DOI
45. Popov, V. Carbon nanotubes: properties and application. *Mater. Sci. Eng. R. Rep.* **2004**, *43*, 61-102. DOI
46. Dresselhaus, M.; Jorio, A.; Saito, R. Characterizing graphene, graphite, and carbon nanotubes by Raman spectroscopy. *Annu. Rev. Condens. Matter. Phys.* **2010**, *1*, 89-108. DOI
47. Kim, H.; Nam, E.; An, K.; Lim, H. Laboratory-scale plastic upcycling and green growth: evaluating the upcycling of plastic waste into carbon nanotubes from economic and environmental aspects. *Chem. Eng. J.* **2024**, *495*, 153300. DOI

48. Sun, Y.; Liu, D.; Zhang, F.; Gao, X.; Xue, J.; Zheng, Q. Multiscale biomimetic evaporators based on liquid metal/polyacrylonitrile composite fibers for highly efficient solar steam generation. *Nano. Micro. Lett.* **2025**, *17*, 129. DOI PubMed PMC
49. Lin, J.; Zhang, Z.; Lin, X.; et al. All wood-based water evaporation-induced electricity generator. *Adv. Funct. Mater.* **2024**, *34*, 2314231. DOI
50. Liu, Z.; Liu, C.; Ni, A.; et al. Tortuosity regulation of two-dimensional nanofluidic films for water evaporation-induced electricity generation. *Nano. Res.* **2024**, *17*, 6192-202. DOI
51. Liu, Y.; Li, Z.; Wang; L; et al. Surface functional modification for boosting power density of hydrovoltaic devices. *Adv. Funct. Mater.* **2023**, *34*, 2312666. DOI
52. Lim, H.; Kim, M. S.; Cho, Y.; et al. Hydrovoltaic electricity generator with hygroscopic materials: a review and new perspective. *Adv. Mater.* **2023**, *36*, 2301080. DOI